ACS **APPLIED** MATERIALS & INTERFACES

Research Article

Rapid Millifluidic Synthesis of Stable High Magnetic Moment Fe$_x$C$_y$ Nanoparticles for Hyperthermia

Katerina Loizou, Stefanos Mourdikoudis, Andreas Sergides, Maximilian Otto Besenhard, Charalampos Sarafidis, Koichi Higashimine, Orestis Kalogirou, Shinya Maenosono, Nguyen Thi Kim Thanh,* and Asterios Gavriilidis*

Cite This: *ACS Appl. Mater. Interfaces* 2020, 12, 28520−28531

Read Online

ACCESS | Metrics & More | Article Recommendations | Supporting Information

ABSTRACT: A millifluidic reactor with a 0.76 mm internal diameter was utilized for the synthesis of monodisperse, high magnetic moment, iron carbide (Fe$_x$C$_y$) nanoparticles by thermal decomposition of iron pentacarbonyl (Fe(CO)$_5$) in 1-octadecene in the presence of oleylamine at 22 min nominal residence time. The effect of reaction conditions (temperature and pressure) on the size, morphology, crystal structure, and magnetic properties of the nanoparticles was investigated. The system developed facilitated the thermal decomposition of precursor at reaction conditions (up to 265 °C and 4 bar) that cannot be easily achieved in conventional batch reactors. The degree of carbidization was enhanced by operating at elevated temperature and pressure. The nanoparticles synthesized in the flow reactor had size 9−18 nm and demonstrated high saturation magnetization (up to 164 emu/g$_{Fe}$). They further showed good stability against oxidation after 2 months of exposure in air, retaining good saturation magnetization values with a change of no more than 10% of the initial value. The heating ability of the nanoparticles in an alternating magnetic field was comparable with other ferrites reported in the literature, having intrinsic loss power values up to 1.52 nHm^2 kg^{-1}.

KEYWORDS: *continuous synthesis, flow reactor, iron carbide, hyperthermia, magnetic saturation*
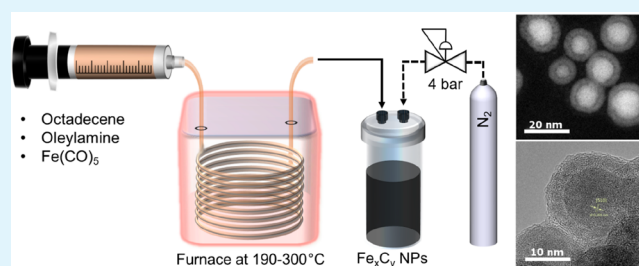
INTRODUCTION

The synthesis of well-controlled magnetic nanomaterials has been of great interest during the past couple of decades as these materials have a plethora of applications in the field of high-density magnetic recording media and biomedical nano-technology.[1−4] In particular, magnetic nanoparticles have been receiving increased attention due to their suitability as therapeutic and diagnostic agents in magnetic resonance imaging (MRI) and magnetic particle imaging (MPI)[5] as well as thanks to their potential for cancer treatment via magnetically induced hyperthermia.[1] Magnetic fluid hyperthermia causes the increase of temperature locally upon application of an alternating magnetic field that can destroy mostly the tumor tissue, without harming surrounding healthy cells.[1,6] The most common magnetic nanoparticles studied for hyperthermia cancer treatment are iron oxide nanoparticles (IONPs). Nevertheless, they display lower magnetic moments than their metallic (nonoxidized) counterparts. Single metal nanoparticles (NPs) such as Fe, Co, or FeCo alloys have much higher magnetic moments, but they are inherently unstable as they are prone to oxidation. Recently, iron carbide nano-particles were given considerable attention for their potential use in biomedical applications.[7] They are reported to offer a trade-off between the stability against oxidation in solution,

which is comparable to iron oxide nanoparticles, while offering superior heating abilities.[8]

The desired properties of magnetic nanoparticles required for their biomedical applications are high magnetic moment, monodispersity, stability against oxidation, and ability for biofunctionalization. As these properties are intrinsically dependent on their size and shape as well as crystal structure and composition, it is crucial that their synthesis is precisely controlled. Magnetic nanoparticles are mostly manufactured in batch from suitable precursors in organic solvents in the presence of surfactant-stabilizing agents and with a reducing agent when necessary.[5,9−11] These synthetic routes offer somewhat limited control over the monodispersity of nano-particles[2] as the inherently fast nucleation and growth associated with thermal decomposition renders these processes hard to control.[12] Additionally, minor variations in reaction conditions can affect the structural characteristics of the
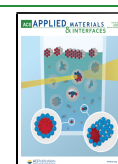
nanoparticles. Thus, there is a need of better control over the synthesis conditions to achieve the desired particle properties.

Continuous flow micro- and millireactors (here referring to the channel diameters) offer excellent homogeneity over reaction conditions as well as tight control over critical parameters, such as the reaction temperature and pressure; therefore, they can enhance synthesis reproducibility. A number of reviews and book chapters have described continuous flow synthesis routes of nanostructured materials. In particular, already in 2008, Kumar and co-workers had reviewed the advances, up to that time, on the microfluidic synthesis of metallic and silica NPs as well as quantum dots.[13] Soon after that, Marre and Jensen discussed the application of microfluidic techniques for achieving size and shape control in the produced nanoparticles (metals, metal oxides, silica, quantum dots, and heterostructures).[14] Luo et al. presented and compared a variety of single-phase and multiphase microfluidic synthetic strategies of NPs.[15] In 2013, Kumar's group highlighted the differences between chip-based as well as millifluidic systems in the synthesis of metal, metal oxide, nanocomposite, and quantum dot nanostructures targeted for biomedical applications.[16] Myers et al. presented the flow chemistry of quantum dots, luminescent hybrid NPs, oxides (ZnO and CeO_2), and metal NPs such as Ag and Au.[17] In 2014, Phillips et al. demonstrated that the use of two-phase flow reactors helped toward improved reaction control, even though the microfluidic reactor was still a long way from displacing the round-bottomed flask as the principal reaction environment for nanocrystal synthesis.[18] Santamaria and co-workers presented several reaction engineering strategies, discussing that a trade-off between maintaining the ability to control the desired nanoscale features and achieving high production rates must be often reached.[19] In another more recent review, Sebastian et al. provided also some examples on the flow synthesis of magnetic NPs (primarily Fe_3O_4-based), which were typically synthesized in relatively moderate temperatures.[20] Other reviews focused mostly on the synthesis of noble metal nanostructures, which are usually synthesized at lower temperatures and are destined typically for applications in catalysis, not excluding other fields.[21−23]

Previous work on the synthesis of magnetic nanoparticles in micro/millifluidic reactors mainly concentrated on the formation of iron oxide nanoparticles via coprecipitation. Typical setups utilized channels or capillary tubes with a critical dimension in the scale of micrometers or millimeters and were broadly categorized in single-phase flow reactors or segmented flow reactors.[12] Several research groups utilized such systems to successfully synthesize monodisperse iron oxide nanoparticles, mostly using the coprecipitation method of two different iron salts.[24−29] Apart from coprecipitation, thermal decomposition is a common method to produce iron-based nanostructures. It involves the chemical decomposition of a precursor at a certain temperature, which is the decomposition temperature of the precursor under certain conditions, thus inducing nucleation. For example, Miyake et al. synthesized Fe_2O_3 fine particles with rather polydisperse size and irregular shape by the decomposition of ferric nitrate nonahydrate in formamide at 150 °C.[30] Concerning the utilization of flow systems to synthesize Fe^0 nanoparticles, there are limited studies because of the high temperatures associated with thermal decomposition of the $Fe(CO)_5$ as well as system limitations in terms of fouling. Recently, Uson et al. successfully synthesized ultrasmall IONPs via a high-temper-

ature synthesis utilizing continuous microfluidic reactors for the thermal decomposition of $Fe(acac)_3$ in tetraethylene glycol (TEG) solution.[31] In another report, the continuous synthesis of ∼7 nm iron oxide NPs was achieved by pumping a precursor solution of presynthesized iron oleate through a stainless steel tubing which was submerged in a salt bath. The reaction temperature employed was up to 340 °C with a 86 min residence time.[32] In another work, the flow synthesis of ∼5 nm IONPs was published by Jiao et al.: their approach involved pumping a precursor solution of $Fe(acac)_3$ via a Hastelloy tubing which was heated to 250 °C and pressurized to 33 bar at the outlet at 0.19−6.6 mL/min. A residence time of 2−30 min was employed.[33]

Herein we demonstrate the continuous synthesis of Fe_xC_y nanoparticles at high temperature and pressure in a millifluidic reactor which performs under inert gas conditions. In addition, our system permits short reaction times as well as efficient heat and mass transfer. The effect of temperature on the size, polydispersity, magnetic response, and magnetic heating efficiency of the synthesized particles is presented. In particular, we illustrate the formation of an iron carbide phase at temperatures >230 °C. The nanoparticles demonstrated good stability against oxidation after 2 months of storage.

■ MATERIALS AND METHODS

Materials. 1-Octadecene (ODE, 90%), oleylamine (OAm, 70%), and iron(0) pentacarbonyl ($Fe(CO)_5$, >99.99%) were obtained from Sigma-Aldrich Ltd., UK. All the reagents were used as purchased without further purification.

Millifluidic System for the Continuous Synthesis of Iron Carbide Nanostructures. The setup employed for the synthesis of magnetic Fe-based nanoparticles is shown in Figure 1. PTFE tubing
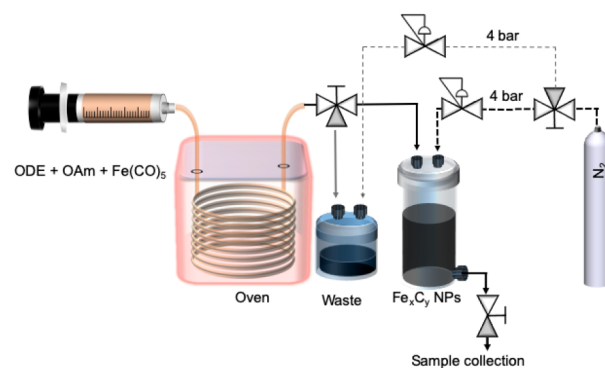
Figure 1. Schematic representation of the setup employed for the continuous synthesis of Fe_xC_y nanoparticles including the chemical reagents used in the reaction (ODE: 1-octadecene; OAm: oleylamine).

and fittings were used to connect the capillary reactor to the syringe in order to introduce the reaction mixture in the reactor. A 4 m long, 0.76 mm internal diameter stainless steel tube was used as a capillary reactor placed in a gas chromatograph oven (Trace GC 2000, ThermoQuest) to achieve temperatures ranging from 190 to 300 °C. At the exit point of the oven the capillary reactor was extended by 10 cm to take advantage of the rapid cooling associated with millifluidic systems. The product then flowed via PTFE tubing to either the waste container or the sample collection vial (PEEK) via a three-way PTFE valve both kept at room temperature during normal operation. Both the waste container and the sample collection vial were kept under pressure during normal operation. The sample was obtained via a PEEK valve connected at the exit of the collection vial.

In a three-neck flask fitted to a Schlenk line, the solvent (ODE, 28 mL) and the stabilizer/surfactant (OAm, 0.34 g, 1.27 mmol) were added. The mixture was degassed under vacuum for 20 min, followed by nitrogen purging for 5 min. The procedure was repeated three times under vigorous magnetic stirring (800 rpm). Afterward, the solution was heated to 120 °C for 30 min under nitrogen flux and vigorous magnetic stirring to remove water through a septum-fitted needle on the side neck of the flask. The mixture was allowed to cool to room temperature. $Fe(CO)_5$ (7.65 mmol) was then injected into the above mixture, following a modified protocol derived by Peng et al.[34]

The precursor solution was pumped through the capillary reactor using a syringe pump (Legato210, KD Scientific) equipped with a 25 mL gastight syringe (SGE syringes, TRAJAN). The reactor outlet was pressurized using a back-pressure regulator (K type, Swagelok) to 4 bar to minimize gas formation. For the experiments presented here, the nominal residence time (based on the reaction mixture inlet flow rate) was fixed at 22 min. The flow rate used for all experiments was 0.083 mL/min, and the reaction temperature varied in the range 190−300 °C. The as-prepared nanoparticles were washed three times with a mixture of hexane and ethanol (1:3 v/v) and isolated by magnetic separation, before being dispersed in hexane.

Batch Synthesis of Iron Carbide Nanostructures. In a three-neck flask fitted to a Schlenk line, the solvent (ODE, 28 mL) and the stabilizer/surfactant (OAm, 0.34 g, 1.27 mmol) were added. The mixture was degassed under vacuum for 20 min, followed by nitrogen purging. After heating at 120 °C, further degassing for 20 min took place. The mixture was then heated at a given temperature (e.g., 250 or 280 °C) at a rate of 5 °C/min under stirring (700 rpm). $Fe(CO)_5$ (7.65 mmol) was injected, and the solution stayed at the same temperature for 20 min. The mixture was allowed to cool at room temperature, and the washing of the particles was done as in the case of the flow-synthesized nanoparticles.

Characterization of the Nanoparticles. The mean size and the morphology of the resulting NPs were investigated by using a JEOL 1200 EX transmission electron microscope (TEM) with a 120 kV acceleration voltage. TEM samples were prepared by depositing a drop of a colloidal dispersion of NPs in hexane onto carbon-coated copper grids. A JEOL JEM-ARM 200F microscope operating at 200 kV with a spherical aberration corrector and a nominal resolution of 0.8 Å was utilized to obtain high-resolution TEM (HRTEM), high-angle annular dark field (HAADF)−scanning transmission electron microscopy (STEM) images and to study the crystallinity and the elemental composition of the as-synthesized NPs, with the aid of energy-dispersive X-ray spectroscopy (EDS).

The crystal structure of the NPs was examined with a PanAlytical X-ray diffractometer (X'Pert Pro) using Co Kα radiation (λ = 1.789010 Å). The diffraction patterns were collected from $2\theta = 20°$ to 100°. Samples were prepared by depositing dried powders of the acquired NPs on a zero-background silicon wafer, which has no background noise from 10° to 120°.

The magnetic properties of the NPs were evaluated by using a vibrating sample magnetometer (VSM) (Model 6000, Physical Property Measurement System, Quantum Design). The magnetic response to a sweeping field was tested at 5 and 300 K. The inorganic metal mass (Fe amount) was identified by measuring the iron content of a dispersion of NPs with known concentration determined via an Agilent 4210 microwave plasma−atomic emission spectrometer (MP-AES).

The heating ability of the NPs was quantified using a calorimetric analyzer (G2 driver D5 Series, nB nanoScale Biomagnetics). This instrument recorded the temperature using a fiber-optic temperature probe immersed into 1 mL of the NP solution in a vial which was placed inside an evacuated sample holder. The sample holder was placed in the center of a current-carrying solenoid generating the alternating magnetic field which was set to a frequency of f = 303 kHz and a field strength of H = 24500 Am^{-1} G. The specific absorption rate (SAR) was determined by using the initial slope after the AC field was applied (dT/dt) by[6]

$$SAR = \frac{C}{m}\frac{dT}{dt}$$

where C is the specific heat capacity of the sample solution (assuming a dilute solution, 4.185 J L^{-1} K^{-1}, as for water) and m is the concentration of iron (g L^{-1}). The SAR [W/kg of iron] value was then normalized with the magnetic field H and frequency f amplitudes used in the measurement to obtain the intrinsic loss power [ILP (nHm^2 kg^{-1})] as defined in[6] (H units: kA/m, f units: kHz)

$$ILP = \frac{SAR}{H^2 \times f}$$

Fe Mössbauer spectra were obtained at room temperature on a conventional constant acceleration spectrometer in transmission geometry operating in a triangular wave mode. The spectrometer contained parts from Wissel (MR-260 drive, MVT-1000 transducer, DFG-500 function generator, LND 45431 gas counter, PEA-6 preamplifier, and AMP-1000 main amplifier), while its recording system was a Canberra PCA-2k. The radiation source consisted of ^{57}Co in rhodium matrix. The isomer shift and the speed scale were calibrated with an α-Fe sample as a reference.
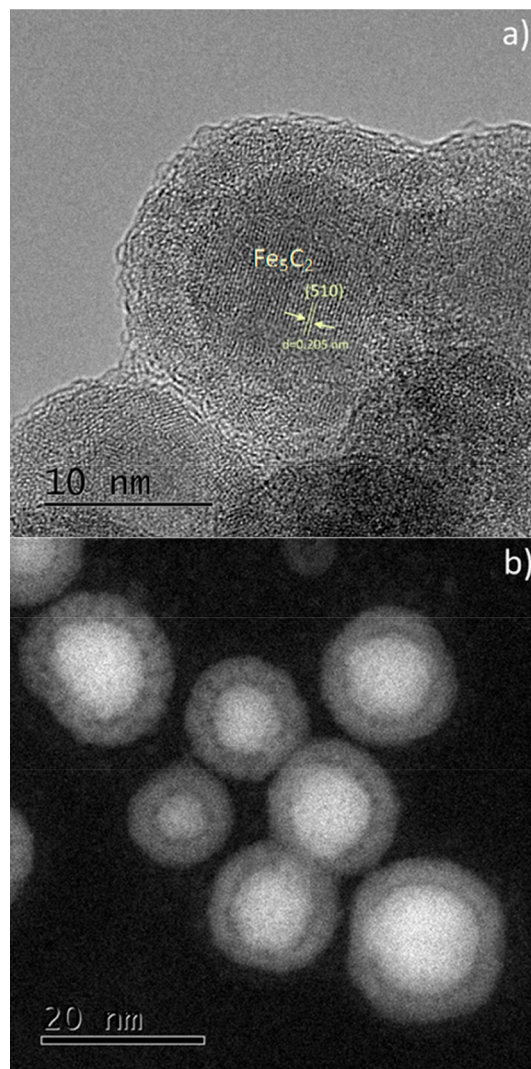
■ RESULTS AND DISCUSSION

Effect of Temperature on the Size of the Nanoparticles. A modified thermal decomposition reaction was employed to synthesize Fe_xC_y nanoparticles. Following the protocol by Peng et al.,[34] $Fe(CO)_5$ was decomposed in a mixture of ODE and OAm, which acts as a ligand in this reaction. In batch syntheses, the method of hot injection is employed, where $Fe(CO)_5$ is injected in a preheated solvent/ligand mixture typically at 180 °C under an inert atmosphere. This system was translated to flow with some modification: all the reactants were premixed under an inert atmosphere and then introduced to the capillary reactor that was heated to the required temperature. In this way the flow reactor mimics a hot-injection method, as widely used for the thermal decomposition of metal carbonyls by employing the extremely rapid heating offered by the flow setup. Temperatures ranging from 190 to 300 °C were tested, while the reactor operated at an elevated pressure of 4 bar. This kept low the volume of the CO generated from the thermal decomposition of $Fe(CO)_5$. It should be noted that at the elevated pressure employed no decomposition was observed at temperatures lower than 190 °C (data not shown). This effect is attributed to a possible alteration of the decomposition temperature of the $Fe(CO)_5$ at the pressure employed under flow conditions.[35,36]

The reaction temperature was varied to evaluate its effect on size, polydispersity, morphology, and resulting magnetic properties of the synthesized nanoparticles. Severe fouling was observed for temperatures over 265 °C, which was attributed to the increased magnetic attraction of nanoparticles synthesized at higher temperatures that leads to partial aggregation: although some particles remain at colloidal state, precipitation of particle aggregates also occurs. At temperatures lower than 265 °C, the reactor operated for more than 1 h continuously, without any pressure buildup that would signify fouling. For the conditions reported here, the TEM images of samples synthesized at 190, 250, and 265 °C are presented in Figure 2 (further images for reaction temperatures of 200, 215, 230, and 240 °C can be found in Figure S1 of the Supporting Information). For all conditions tested, a distinct core−shell morphology was observed, as can be seen more clearly at the HRTEM image of Figure 3, indicating the formation of an iron oxide layer upon exposure of the nanoparticles to air. It is noteworthy that sizes reported
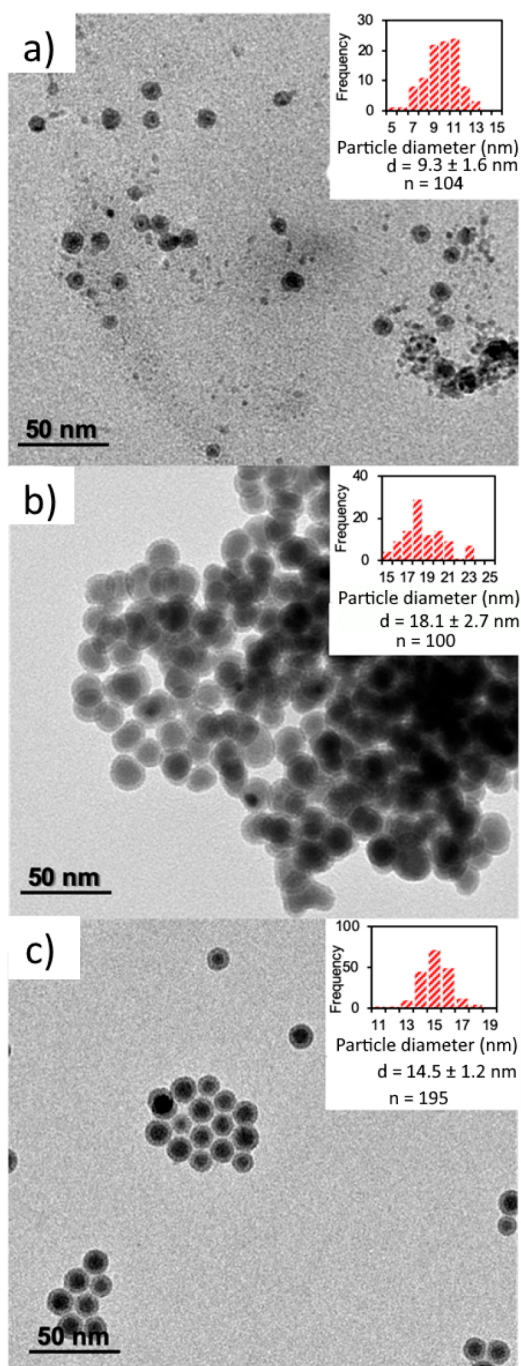
Figure 2. (a−c) TEM images with size and size distributions of nanoparticles (insets) synthesized at 190, 250, and 265 °C, respectively. *d* is the diameter of the nanoparticles measured from the TEM images, and *n* is the number of nanoparticles measured for each histogram.

Figure 3. (a) HRTEM and (b) STEM images for nanoparticles synthesized at 265 °C.

here correspond to the total diameter of the core−shell nanostructures, accounting for both the shell and the core. The NP size increased with temperature up to 250 °C. The mean diameter of the resulting nanoparticles synthesized at 190 and 200 °C was measured to be 9.3 ± 1.6 and 9.9 ± 1.8 nm, respectively. Further increase of the temperature to 215 and 230 °C resulted in an increase of the mean diameters to 13 ± 2.1 and 14.7 ± 2.4 nm, respectively. When the reaction temperature was increased even more, the size of the resulting nanoparticles appeared to reach a maximum at 250 °C, where the mean diameter was 18.1 ± 2.7 nm. At 265 °C, the highest temperature tested where no catastrophic fouling was observed, the NP size decreased to 14.5 ± 1.2 nm.

It should be noted that the relative standard deviation (RSD) of the size (defined as the ratio between the standard deviation of the particle size distribution over the mean diameter) was below 20%; the sample synthesized at a reaction temperature of 265 °C had an RSD of 8.3%. It is suggested that increasing the reaction temperature leads to an increase of the mean size of the nanoparticles, as according to Wen et al., at higher temperatures the nucleation rate of iron nanoparticles is reduced due to the lack of a quick consumption pathway of the Fe atoms formed.[37] Therefore, because of the fast decomposition of $Fe(CO)_5$ and a reduced number of nuclei present, any Fe atoms formed are used to produce larger clusters.[37] It should be noted that nanoparticles synthesized in our reactor at temperatures higher than 240 °C were prone to aggregation.

As seen in Figure 4, batch reactions performed at higher temperatures indicate that smaller particles were generated compared to those in the millifluidic system. Batch experiments reported by Peng et al.[34] showed the formation of nanoparticles with a mean diameter of 6.5 nm via the thermal decomposition of iron carbonyl in octadecene at 180 °C. Our
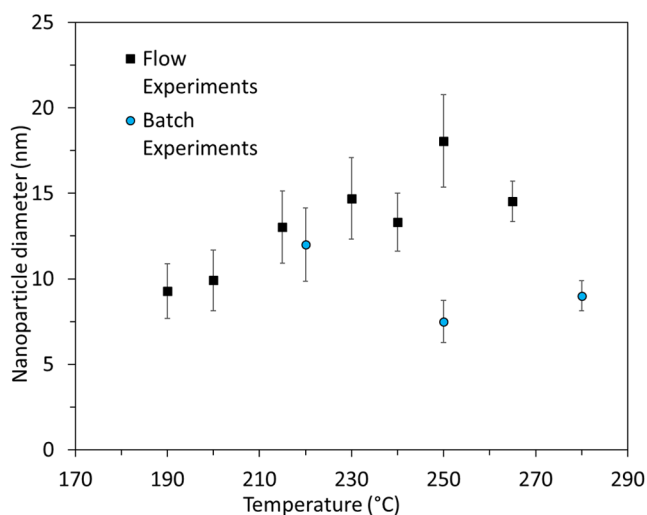
Figure 4. Nanoparticle diameters obtained as a function of reaction temperature for both flow and batch experiments. The standard deviation of the mean diameter is plotted as error bars.

system has the ability to synthesize larger nanoparticles with good size control and high magnetic properties, as shown in the following sections. To shed light on the different results between the two systems (batch and flow), one should consider the mechanism of nanoparticle formation. In batch, when the carbonyl precursor is injected in the hot solution, it is rapidly decomposed to form a large number of nuclei. When a critical concentration of nuclei is attained, Fe atoms are subsequently deposited on the formed nuclei resulting in growth of the nuclei to clusters and then to nanoparticles, as described by the LaMer model.[36] However, in the millifluidic reaction system, it is hypothesized that the pressure applied on the system has a suppressing effect on the thermal decomposition rate of the $Fe(CO)_5$.[36] Therefore, the number of nuclei formed is smaller than that in a batch system operated at atmospheric pressure. Thus, the delayed thermal decomposition of the $Fe(CO)_5$ due to the increase in pressure led to the formation of larger nanoparticles in the flow system compared to batch. In addition, it seems that the increase of temperature, at least up to 250 °C, was associated with a reduction of the nucleation rate, as mentioned above,[36] resulting in a size increase. The reactor yield and the productivity in mg_{Fe}/min are reported in Table S1.

In terms of scalability in this case the most relevant option would be to increase the diameter of the reactor up to the critical diameter where the associated hydrodynamics and heat transfer is not affected. In case of need for further scaling up, the scaling out of the designed reactor can be considered. The current setup can accommodate several reactors in parallel, thus permitting the scaling up in numbers, that altogether could reach a production of a few hundreds of milligrams of nanoparticles in less than an hour of synthesis. In this manner the scale of nanoparticle production can be significantly increased without compromising the heat and mass flow control of the system.

Effect of Temperature on the Chemical Composition and Crystal Structure of the Nanoparticles. It was found that increasing reaction temperature produced NPs with higher crystallinity as seen in the XRD patterns of three representative samples synthesized at various temperatures (Figure S2). Reaction temperatures below 190 °C did not produce any NPs

under flow conditions. In the literature, batch synthesis at 180 °C caused the formation of mainly amorphous NPs.[34] In our work, the peaks for the sample produced at 215 °C imply a rather low degree of crystallinity, while the samples synthesized at higher temperatures have sharper XRD peaks. The XRD measurements were performed a few hours after the synthesis to minimize the particles contact with air, as Fe is extremely sensitive to oxidation. In fact, the signal of the NPs prepared at 215 °C is quite noisy, while the measurements of the NPs synthesized at 230 and 265 °C seem to denote the simultaneous presence of iron carbides and Fe_3O_4.

To perform a better phase-composition analysis of the samples synthesized at 230 and 265 °C, Rietveld refinement of the XRD patterns was performed using the FullPROF software (Figure 5).[38] According to the Rietveld analysis, the primary
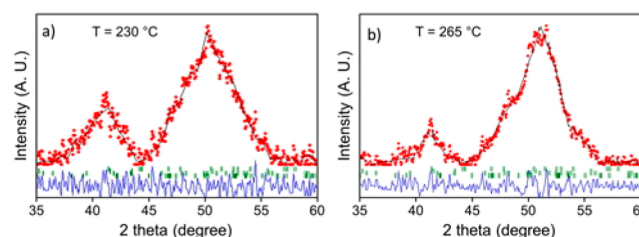
Figure 5. Rietveld refinement of the powder XRD patterns of samples synthesized by flow synthesis at (a) 230 and (b) 265 °C. The experimental patterns are shown as red circles and the calculated patterns as black lines. The Bragg reflection positions for iron carbide and magnetite components are shown as short green bars below the diffraction patterns (see also Figure S3). Blue lines represent the difference patterns.

phase of both samples is found to be Fe_5C_2 and the secondary phase is Fe_3O_4 (Figure S3). However, the χ^2 values are 16.9 and 14.7 for the samples synthesized at 230 and 265 °C, respectively. In general, it is regarded that the Rietveld refinement is very satisfactory when $\chi^2 < 4$. The reason for the ill fit is mainly due to the peak broadening. It has to be noted that a significant percentage of magnetite may be present in an amorphous state and cannot be detected by XRD (which determines only crystallite entities).

The XRD measurements were performed a few hours after synthesis, which would possibly justify a relatively low degree of oxidation (especially the sample prepared at 230 °C was measured at XRD right after its washing and drying procedure, and the sample of 265 °C followed a few hours later). It seems that the formation of an oxide layer was very fast, and it took place soon after particle synthesis, as suggested also by the brighter contrast of the outer shell of the particles at the TEM (acquired 2 days after synthesis) and HRTEM images (Figures 2 and 3). The main finding of the XRD analysis is that the increase of synthesis temperature seems to favor the formation of iron carbide phases, since the sample synthesized at 215 °C does not show any clear sign of crystallinity or carbidization (Figure S2). Figure S3 includes also the simulated reference patterns for the different carbide compositions and magnetite together with the XRD measurements for the two samples prepared at 230 and 265 °C. Iron carbides are normally regarded as metallic crystals with interstitial carbon atoms. Our observation of the generation of iron carbide phases at high temperatures is in agreement with the literature, for instance with a report using octadecylamine (ODA), cetyltrimethyl-

ammonium bromide (CTAB), and iron pentacarbonyl in a batch synthesis.[39] In our case, the organic medium used in the synthesis, composed of ODE and OAm, was the source of carbon atoms. In another work, Yang et al. used ODE, ODA, OAm, NH_4Br, and $Fe(CO)_5$ in their batch synthesis, similarly reporting that higher temperatures favor the production of carbon-rich phases.[40]

It is interesting to note that these authors state that the carbidization process results in slightly larger nanoparticle sizes (a conversion of body-centered-cubic Fe—also known simply as bcc-Fe or α-Fe—to hexagonal-Fe_2C resulted in an average size increase from 14.0 to 14.9 nm). This was due to a lattice distortion caused by C atom penetrations, which expanded the whole particle volume; this tendency for size increase during the carbidization process is in agreement with our TEM results, although in our case this tendency is even more profound.[40] Other reports, for example by Schaak and colleagues in the case of Ni-based NPs, have demonstrated that reaction time is another parameter, apart from reaction temperature, that can be tuned for the synthesis of metal carbides (in that case, Ni_3C_{1-x}).[41]

Although the peak deconvolution of the XRD measurements helped us to get a better idea of the samples composition and confirmed the presence of iron carbides and magnetite, the numerous phases of possible iron carbide structures in nearby peak positions made necessary to employ additional characterization techniques. In particular, the HRTEM image of an isolated Fe_5C_2 nanoparticle from the 265 °C sample (Figure 3a) reveals its characteristic core−shell structure, with a clear contrast between the core and the shell regions. The lattice spacing in the core was measured at ≈0.205 nm, attributed to the (510) plane of Fe_5C_2. The shell seems to consist of amorphous entities with numerous small crystalline domains, in principle attributed to magnetite, taking into account the XRD measurements. Amorphous carbon, crystalline Fe_3O_4, or even a mixture of amorphous and crystalline phases of iron oxides has been reported to compose the shell around the iron carbide core in several cases in the literature.[39,40,42] The STEM image at Figure 3b corroborates the core@shell structure whereas a careful look at the EDS elemental mapping (Figure 6) reveals that the core is rather Fe-rich, as expected, and the O is mostly located at the outer layers of the NPs.

Carbon is abundant in the whole particle volume because of the presence of the surfactant (OAm) and possibly also due to the existence of traces of solvent (ODE), despite thorough washing, and due to the use of a C-coated TEM grid. Similar observations can be made for the sample synthesized at 230 °C (Figure S8; for example, in Figure S8d a Fe-rich core can be barely noticed). In our samples, the presence of a tiny void layer between the Fe-rich iron carbide core and the shell is faintly observed in the STEM images. Such void space has been suggested to act as a possible reactive zone for the carbon penetration process, indicating the occurrence of a Kirkendall effect through the lattice transition. The Kirkendall effect is manifested through the void formation caused by the imbalance of diffusion rates, when cations diffuse outward to react with reactive anions. According to this effect, atomic diffusion occurs through vacancy exchange and not by the direct interchange of atoms. The generation of numerous hollow materials in the nanoscale has been described through this effect.[40,43]

Although XRD and HRTEM shed some light on the composition of our samples, the particles' composition was not
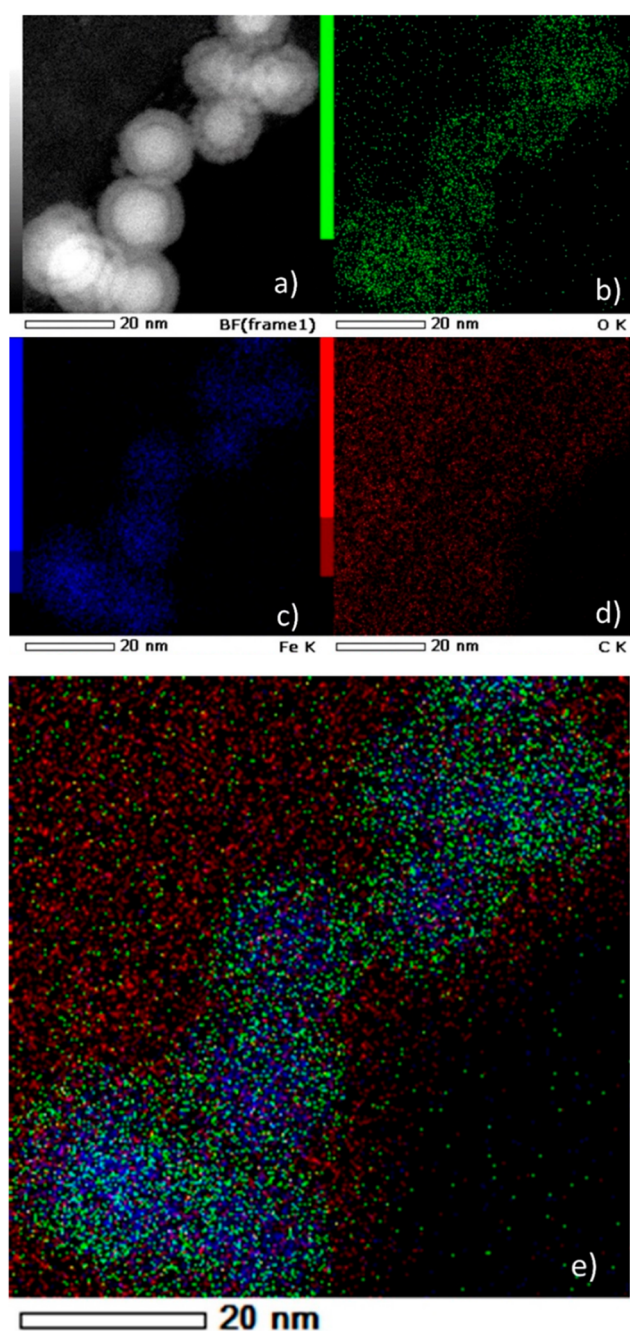
Figure 6. (a) HAADF-STEM bright-field image. (b−e) EDS elemental mapping images of the nanoparticles synthesized at 265 °C: (b) O K edge, (c) Fe K edge, (d) C K edge, and (e) overlay.

fully conclusive based on those measurements alone. An advantage of the XRD measurements is that they examine the whole population of a powder sample. However, in our case, not all XRD peaks can be assigned clearly to specific crystal phases. HRTEM is more precise when studying the crystal structure of individual particles, but it suffers from the fact that it is not macroscopic, as it only studies a limited number of particles. Also, if some NPs are polycrystalline or consisting of small crystalline domains, it becomes quite difficult to identify their composition by HRTEM alone. Therefore, we used Mössbauer spectroscopy to examine the samples further. This technique is one of the powerful tools to discriminate Fe, Fe oxide, or Fe carbide phases in the complex metastable Fe_xC_y

system.[44] ^{57}Fe Mössbauer spectra were collected at room temperature for the samples synthesized at 265 and 230 °C, and they are presented in Figure 7.
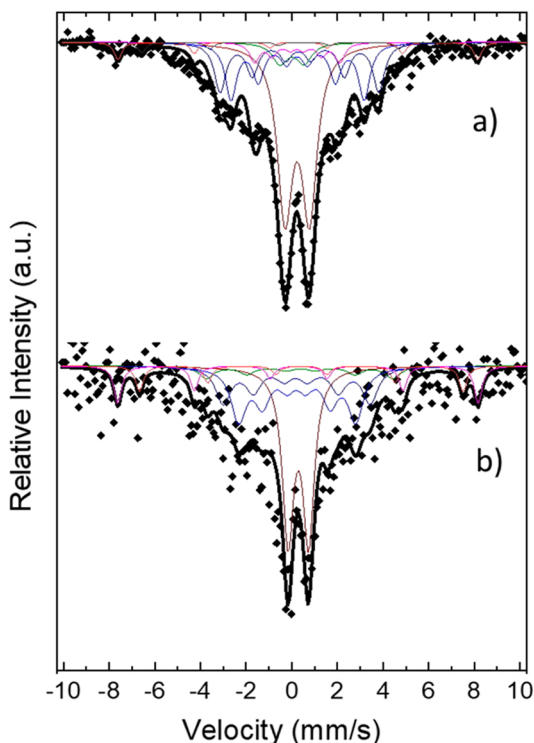
Figure 7. Mössbauer spectra for the sample synthesized at (a) 265 and (b) 230 °C. Colored subspectra for the main individual sextets which contribute to the overall spectrum are included, one for each Fe species in different crystallographic position as shown in Tables 1 and 2.

Many different models were applied to obtain the best fit. For the 265 °C sample a composite model that included χ-Fe$_5$C$_2$ and magnetite Lorentzian sextets gave the best results. As seen from the shape of the large central peaks, two doublets with nonzero and distributed quadruple splitting were necessary to fit the spectrum. They may be attributed to unreduced paramagnetic ferrous ions or size-induced super-paramagnetic relaxation effects. The carbide can be described with three sextets corresponding to three different Fe crystallographic positions for the Fe ions. According to the population of the ions, a 2:2:1 area ratio of the total three sextets area is expected, and the obtained relative areas for χ-Fe$_5$C$_2$ were 2:2:0.7, which are close to the theoretical values. Hyperfine fields (B_{HF}) for the sextets were close to the literature[45−48] with a normalized average value of 18.5 T, which is lower than α-Fe due to the Fe−C bonds. Both isomer shift (δ) and quadruple splitting (ε) were slightly smaller, with average values of 0.27 and 0.04 mm/s, respectively. The isomer shift value is relative to α-Fe and is related to the s electrons' density on the nucleus, which in turn is affected by the oxidation state of Fe atoms: a smaller isomer shift relates to lower Fe oxidation state. Magnetite sextet parameters were kept constant during the fit apart from the density areas only to be released in the final fit stages. The weight ratio between the two phases (Fe$_5$C$_2$ and magnetite) was found to be 5:1 for the 265 °C sample.

The proportion of magnetite cannot be estimated with high certainty with the Rietveld study for three reasons: (a) The samples were measured just after their synthesis, washing, and drying stages, within a few hours. Possibly during this time they were not oxidized to a significant degree, while Mössbauer analyses were performed 2 months after synthesis. (b) Mössbauer analysis can also detect the noncrystalline iron oxides, unlike XRD which can identify only the crystalline phases. (c) The peak broadening at the XRD patterns induces an uncertainty factor in the Rietveld analysis, and thus the actual percentage of magnetite cannot be precisely determined through that method. The possibility for the presence of traces of other carbide phases could be barely suggested by the Rietveld analysis, but this was not confirmed by Mössbauer analyses. In both measurements, the dominant iron carbide phase is the Fe$_5$C$_2$, in accordance also with the HRTEM.

The fact that Fe is extremely prone to oxidation resulted in the lack of any evidence for possible Fe(0) presence among our samples. With regard to the presence of iron carbides, Yao et al. reported that only at temperatures above 310 °C iron carbides could be formed, when decomposing Fe(CO)$_5$ in a mixture of octadecylamine and CTAB. Octadecylamine is in liquid form at high temperatures and acted as the solvent (apart from its surfactant role).[39] In a similar synthetic process, Hou and co-workers reported the synthesis of Fe$_5$C$_2$ NPs at 350 °C,[42] whereas Ma and coauthors showed also that similar high temperatures are indeed needed for the generation of iron carbides.[51] In a very recent work, Tzitzios and co-workers reported that carbidization took place at reaction temperatures higher than 300 °C for Fe$_3$C nanostructures prepared in oleylamine in the presence of Fe(acac)$_3$, palmitic acid, and 1,2-hexadecanediol.[52]

Wheatley and colleagues presented a two-step protocol that involved the use of Fe seeds, with otherwise similar reagents as in our work (iron pentacarbonyl, oleylamine, and octadecene), and they synthesized Fe@Fe$_3$O$_4$ NPs without observing any carbide phase for reaction temperatures up to 250 °C.[53] In another report, iron carbides could be synthesized at 260 °C, employing a seed-mediated route involving bcc-Fe NPs as seeds, in the presence of long-chain alkylamines and halides.[40]

Table 1. Hyperfine Parameters of the Mössbauer Spectra of the Nanoparticles Synthesized at 265 °C

	δ (mm/s)	ε (mm/s)	B_{HF} (T)	W (mm/s)	area per Fe site (%)	area per phase (%)
doublet	0.24	1.08		0.40	38	
doublet	0.01	1.06		0.40	6	
Fe$_5$C$_2$	0.24	0.03	18.1	0.30	21	47
	0.31	0.05	21.6	0.30	19	
	0.23	0.02	11.6	0.25	7	
magnetite	0.28	−0.02	49.0	0.20	6	9
	0.55	0.01	44.3	0.20	3	

It seems that our synthetic process in flow provides conditions that allow to initiate the carbidization process at temperatures as low as 230 °C, even without the use of halides. It is expected that in the closed flow system the solubility of CO in octadecene is increased compared to a conventional batch system due to the elevated pressure. Because the amount of iron pentacarbonyl used was 7.65 mmol, the concentration of CO cannot exceed 0.0382 mol/L (calculated taking into

Table 2. Hyperfine Parameters of the Mössbauer Spectra of the Nanoparticles Synthesized at 230 °C

	δ (mm/s)	ε (mm/s)	B_{HF} (T)	W (mm/s)	area per Fe site (%)	area per phase (%)
doublet	0.25	1.01		0.40	38	
Fe_5C_2	0.22	0.04	17.7	0.30	18	46
	0.26	0.04	22.3	0.30	18	
	0.19	0.03	13.5	0.25	10	
magnetite	0.29	−0.06	49.5	0.20	10	16

account the decomposition of the $Fe(CO)_5$ molecule, the residence time, and the dimensions of the reactor). Because of lack of data in the literature for Henry's law constant for CO in 1-octadecene, the CO solubility was compared to that in 1-octene, heptane, and hexadecane, as seen in Figure S9. Using this information, we estimated the solubility of CO to be 0.02−0.04 mol/L. Figure S9 supports that the solubility of CO at the lower CO partial pressures encountered in batch systems is significantly smaller than at higher partial pressures, assuming that CO is the only gas present. Therefore, it is postulated that in our millifluidic system the increased amount of CO present might enhance the carbidization at lower temperature, acting as an additional carbon source (apart from OAm). The suggested pathway for the formation of the core−shell morphology includes first the decomposition of iron pentacarbonyl to provide Fe(0), and a subsequent carbidization step yields Fe_5C_2 NPs. The latter is caused by penetration of carbon atoms into the α-Fe lattice, which can also result in lattice distortion. In our case, oleylamine acts as the main carbon source in high temperatures.[40,52] It is worth mentioning that in other works a more complicated structural evolution of

iron species has been shown to be responsible for the generation of Fe_5C_2 NPs: an intermediate FeO phase has also been observed in the course of the synthetic reaction; however, that work involved batch synthesis with much lower heating rate in comparison to our flow conditions.[39] With regard to the passivating oxide shell, as discussed before, it is formed as soon as the particles are exposed to air. Similarly, in our previous work on $Fe@Fe_xO_y$ NPs, no change in the core−shell structure was observed by TEM a few months after synthesis.[54] The synthetic approach by Chaudret and co-workers, which usually includes H_2 reduction and moderate temperatures (150 °C), can also result in the formation of different iron carbide NPs with compositions such as Fe_5C_2 and $Fe_{2.2}C$.[55,56] Their approach involves reactions that last many hours, up to 48 h or more. As mentioned before, a prolonged reaction time is another factor that has also been shown to favor the carbidization process, apart from the high temperature.[41]

Magnetic Properties of the Nanoparticles. The magnetic response of the NPs synthesized at temperatures 230−265 °C was analyzed via VSM within 1 week of formation. Samples formed at lower temperatures (<230 °C) did not show any magnetic response when tested by using VSM. This can be attributed to the fact that those NPs were potentially fully oxidized before the VSM measurement was performed as a result of their amorphous structure,[51] which was demonstrated by XRD measurements. Their smaller size, with a higher surface-to-volume ratio, compared to the samples synthesized at higher temperatures, may also have somewhat contributed as a secondary factor to their tendency to oxidize easily. Therefore, VSM measurements were performed for samples synthesized at higher temperatures, and the results are shown in Figure 8. For the lowest decomposition temperature
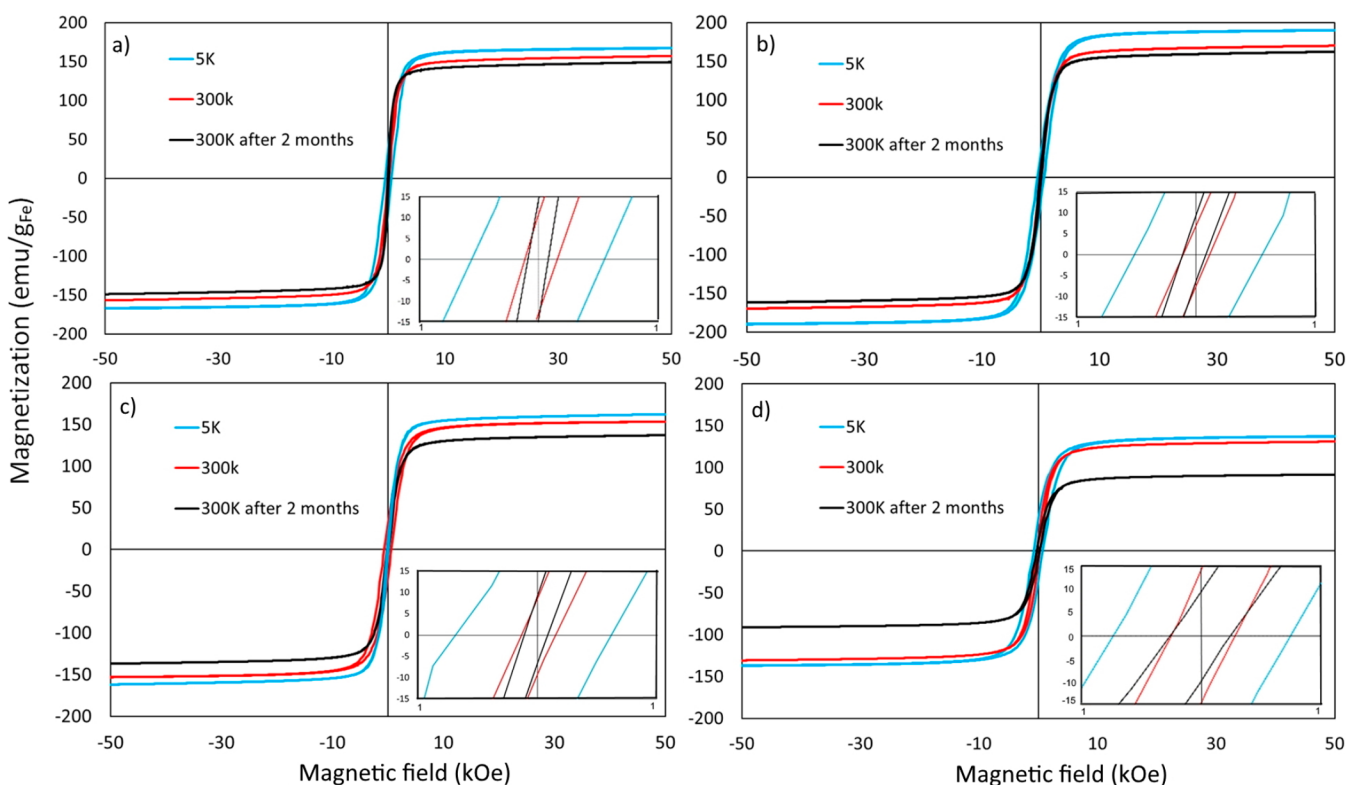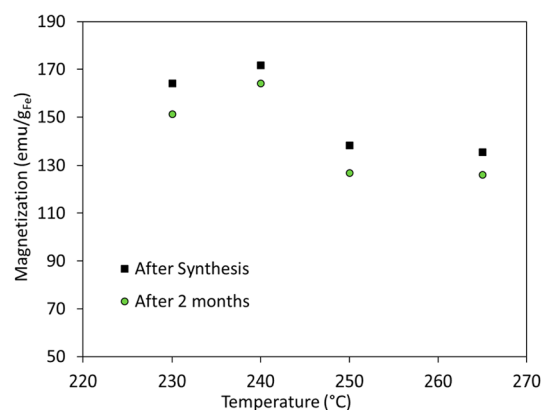

Figure 8. Magnetization measured at different temperatures and at different time intervals plotted against the magnetic field for the nanoparticles synthesized at (a) 230, (b) 240, (c) 250, and (d) 265 °C. The insets show the hysteresis loop at low fields.

of 230 °C the saturation magnetization (M_s) value measured at room temperature was 157 emu/g_{Fe} (92 emu/g_{sample}). An increase of the reaction temperature to 240 °C led to a magnetic saturation value of 167 emu/g_{Fe} (101 emu/g_{sample}). However, further increase of the reaction temperature to 250 and 265 °C resulted in a decrease of the magnetic saturation, with values for samples synthesized at these temperatures plateauing at 138 emu/g_{Fe} (97 emu/g_{sample}) and 136 emu/g_{Fe} (100 emu/g_{sample}). The observed decrease of the Fe content-normalized magnetic saturation values for samples synthesized at higher temperatures can be attributed to the high degree of carbidization of the NPs. As discussed above, increasing the reaction temperature results in the formation of iron carbide phases. This effect is more prominent at the two highest reaction temperatures, and this is reflected in the magnetic saturation values measured. The trend of the magnetic saturation value is in agreement with results presented by Meffre et al.,[55] who observed a decrease in the magnetic saturation values in the case of iron carbides compared to Fe(0) samples. Our iron carbide NPs show higher magnetic saturation values than magnetite, in agreement with literature reports. For example, iron carbide NPs have demonstrated saturation magnetization values of 125−140 emu/g_{sample}, while the corresponding values for magnetite and α-Fe are 70−80 and up to 200 emu/g_{sample}, respectively.[40,42,51,57,58] Especially for the bulk Fe_5C_2, a M_s value of 143 emu/g_{sample} has been reported.[59]

In what concerns the coercivity exhibited by the four samples presented, its value tends to increase with increasing reaction temperature. The measured coercivity was 121 Oe for the NPs synthesized at 230 °C, while it decreased to 72 Oe for the NPs synthesized at 240 °C. Further increase of the reaction temperature to 250 and 265 °C resulted in increasing the measured coercivity value to 151 and 254 Oe, respectively. This increase can be attributed to the increase of the carbon content. The dependence of coercivity on the C content has been reported by Meffre et al.[55] and Yu et al.[58] In particular, a minimum coercive field of ~150 Oe at an iron percentage composition near 80% was found for iron carbide-based NPs.[55] In addition, the coercivity is size dependent.[53] No exchange coupling is noticed because both iron carbide and iron oxide phases are soft magnetic materials with comparable coercivity values in the nanoscale.[60]

The stability of the resulting NPs was also examined. VSM measurements were performed 2 months post synthesis. Results in Figure 9 demonstrate that the magnetization saturation values for all samples decreased by <10% of the original value. These relatively stable magnetic properties may be attributed to the formation of iron carbide phases. As iron carbide displays higher stability against oxidation, the magnetic saturation values are not significantly affected when the samples are exposed in air even for 2 months. It has to be noted that such iron carbide nanoparticles are stable against oxidation despite the fact that they are in a zerovalent state.[40,52,53] It seems that the fast formation of the oxide shell as soon as the particles are exposed to air "passivates" the surface of the NPs, hindering further oxygen insertion into the iron carbide core. In this way, good magnetic properties are kept for prolonged time.[8,55,56] It has been proposed that the formation of a polycrystalline Fe-based shell and the presence of a carbonaceous interface between the shell and the iron carbide core prevent epitaxial growth of the latter and provide a barrier against its further oxidation.[53] In contrast, the

Figure 9. Magnetization values of different samples plotted against the reaction temperature. Measurements were performed at room temperature.

environmental oxidation of Fe NPs would be mostly expected to yield an epitaxial metal−oxide boundary. For example, purely amorphous Fe NPs are very easily oxidized.[51] While it is not that clear how the passive oxidation of the iron carbide core proceeds to generate carbonaceous material internal to the particle structure, the entrapment of OAm from the ligand coating is believed to be involved.[53]

Magnetic Hyperthermia Performance of the Nanoparticles. The heating ability of the synthesized nanoparticles was evaluated via magnetic hyperthermia measurements during the exposure to AC (alternating current) magnetic fields, and the results are summarized in Table 3. It is apparent that an

Table 3. Specific Absorption Rate and Intrinsic Loss Power Values for the Nanoparticles Synthesized at Different Temperatures in the Millifluidic Reactor

reaction temp (°C)	specific absorption rate, SAR (W g^{-1})	intrinsic loss power, ILP (nHm² kg^{-1})
230	30.8	0.17
240	49.3	0.27
250	18.7	0.10
265	278.1	1.52

increase in the reaction temperature resulted in higher ILP values of nanoparticle solutions, measured directly upon collection from the reactor. The magnetic hyperthermia measurements were repeated twice for each sample, and the RSD was <5% for all samples. The values presented correspond to the heating efficacy of nanoparticles dispersed in ODE (reaction solvent). The highest ILP value of 1.52 nHm² kg^{-1} was obtained for the sample prepared at the highest reaction temperature (265 °C). Recent work published by Asensio et al.[61] has highlighted the effect of agglomeration on the heating properties of iron carbide NPs. The authors commented on the absence of heating properties for nanoparticles that are strongly and irreversibly aggregated. However, this was not apparent in the properties of the iron carbide NPs in our work. Even though aggregation was observed for samples synthesized at temperatures higher than 240 °C, nanoparticles demonstrated sufficient heating performance.

Differences between the observed heating properties could be attributed to the different particle sizes and carbidization extents among the different samples. Furthermore, the

significant increase of the SAR value and thus of the ILP value for the sample synthesized at 265 °C can be correlated to the decreased particle size distribution, as the heating efficiency of NPs significantly decreases with any increase of the polydispersity.[62,63] Comparing the magnetic hyperthermia performance of our nanoparticles with different core−shell ferrite nanoparticles from the literature, we observed that the ILP value measured for the particles synthesized at 265 °C is higher than the ILP values reported for core−shell nanoparticles $CoFe_2O_4$ and $MnFe_2O_4$ (0.6 nHm^2 kg^{-1}) for core sizes of 9 and 15 nm, respectively.[56] The SAR value for the sample synthesized at 265 °C is comparable to the SAR values of other reports on iron carbide nanoparticles, as shown in a review by Yu et al. In that review, SAR values between 250 and 300 W g^{-1} or somewhat higher than 300 W g^{-1} were reported for iron carbide and iron oxide/iron carbide core/shell nanostructures, respectively.[58] We tested also the heating ability of our batch-prepared nanoparticles. The samples prepared at 250 °C with both methods (batch and flow) showed similar heating efficiencies. In what concerns the samples synthesized at the highest temperatures (280 °C for batch, 265 °C for flow), a considerably lower ILP value was noticed for the batch sample (Table S2), in comparison to the flow sample (Table 3). It seems that above 250 °C a combination of larger particle size (see Figure 4) and a probably higher degree of carbidization for the flow-prepared sample is responsible for the remarkable differences of the ILP values between the samples synthesized from the two methods (1.52 vs 0.34 nHm^2 kg^{-1}, respectively). The sample synthesized at 220 °C in batch showed a tendency to sedimen easily during hyperthermia measurements, probably due to its relatively big particle size; therefore, unfortunately its performance could not be evaluated in a reliable way.

CONCLUSIONS

In this study, we have investigated the synthesis of Fe_xC_y nanoparticles in a continuous millifluidic system. The effect of the reaction temperature on the size, morphology, and magnetization of the produced nanoparticles has been presented. Results demonstrate that increasing the reaction temperature for the flow system that operates under pressure leads to increasing the diameter of the nanoparticles. Despite the fact that a higher amount of dissolved CO could impede particle growth, we did not observe any such effect in our flow system, although a weak size decrease at 265 °C was noticed after a size maximum at 250 °C synthesis temperature. Still, flow-prepared particles had a larger size compared to batch-prepared ones. Additionally, an iron carbide phase was partially formed at temperatures as low as 230 °C. Increasing the reaction temperature resulted in an enhanced degree of carbidization, as demonstrated by XRD and Mössbauer measurements. A naturally formed passivating oxide layer helped to maintain a stable core−shell morphology for a prolonged time with associated practically intact magnetic properties. The synthesized nanoparticles had ILP values up to 1.52 nHm^2 kg^{-1} measured directly upon collection in 1-octadecene. Only a <10% drop of the initial magnetic saturation after 2 months of air exposure was observed, rendering these particles suitable for different applications that dictate a longer shelf life.

ASSOCIATED CONTENT

Supporting Information

The Supporting Information is available free of charge at https://pubs.acs.org/doi/10.1021/acsami.0c06192.

TEM images, XRD plots, HRTEM-STEM-EDS figures, and solubility data for carbon monoxide (PDF)

AUTHOR INFORMATION

Corresponding Authors

Asterios Gavriilidis − *Department of Chemical Engineering, University College London, London WC1E 7JE, U.K.;* orcid.org/0000-0003-3508-5043; Email: a.gavriilidis@ucl.ac.uk

Nguyen Thi Kim Thanh − *Biophysics Group, Department of Physics and Astronomy, University College London, London WC1E 6BT, U.K.; UCL Healthcare Biomagnetic and Nanomaterials Laboratories, London W1S 4BS, U.K.;* orcid.org/0000-0002-4131-5952; Email: ntk.thanh@ucl.ac.uk

Authors

Katerina Loizou − *Department of Chemical Engineering, University College London, London WC1E 7JE, U.K.;* orcid.org/0000-0003-4487-3834

Stefanos Mourdikoudis − *Biophysics Group, Department of Physics and Astronomy, University College London, London WC1E 6BT, U.K.; UCL Healthcare Biomagnetic and Nanomaterials Laboratories, London W1S 4BS, U.K.;* orcid.org/0000-0001-7187-5128

Andreas Sergides − *Biophysics Group, Department of Physics and Astronomy, University College London, London WC1E 6BT, U.K.; UCL Healthcare Biomagnetic and Nanomaterials Laboratories, London W1S 4BS, U.K.;* orcid.org/0000-0003-0022-3258

Maximilian Otto Besenhard − *Department of Chemical Engineering, University College London, London WC1E 7JE, U.K.;* orcid.org/0000-0002-5079-617X

Charalampos Sarafidis − *Department of Physics, Aristotle University of Thessaloniki, 54124 Thessaloniki, Greece;* orcid.org/0000-0002-5990-0973

Koichi Higashimine − *School of Materials Science, Japan Advanced Institute of Science and Technology, Nomi, Ishikawa 923-1292, Japan*

Orestis Kalogirou − *Department of Physics, Aristotle University of Thessaloniki, 54124 Thessaloniki, Greece;* orcid.org/0000-0002-4078-8168

Shinya Maenosono − *School of Materials Science, Japan Advanced Institute of Science and Technology, Nomi, Ishikawa 923-1292, Japan;* orcid.org/0000-0003-2669-8219

Complete contact information is available at:
https://pubs.acs.org/10.1021/acsami.0c06192

Notes

The authors declare no competing financial interest.

■ REFERENCES

(1) Thanh, N. T. K. *Magnetic Nanoparticles: From fabrication to clinical applications*; CRC Press: Boca Raton, FL, 2012.

(2) Thanh, N. T. K. *Clinical Applications of Magnetic Nanoparticles*; CRC Press: Boca Raton, FL, 2018.

(3) Medina-Sánchez, M.; Miserere, S.; Merkoçi, A. Nanomaterials and lab-on-a-chip technologies. *Lab Chip* 2012, 12, 1932−1943.

(4) Lacroix, L. M.; Frey Huls, N.; Ho, D.; Sun, X.; Cheng, K.; Sun, S. Stable single-crystalline body centered cubic Fe nanoparticles. *Nano Lett.* 2011, 11, 1641−1645.

(5) Cheong, S.; Ferguson, P.; Hermans, I. F.; Jameson, G. N.; Prabakar, S.; Herman, D. A.; Tilley, R. D. Synthesis and stability of highly crystalline and stable iron/iron oxide core/shell nanoparticles for biomedical applications. *ChemPlusChem.* 2012, 77, 135−140.

(6) Kallumadil, M.; Tada, M.; Nakagawa, T.; Abe, M.; Southern, P.; Pankhurst, Q. A. Suitability of commercial colloids for magnetic hyperthermia. *J. Magn. Magn. Mater.* 2009, 321, 1509−1513.

(7) Hervault, A.; Thanh, N. T. K. Magnetic nanoparticle-based therapeutic agents for thermo-chemotherapy treatment of cancer. *Nanoscale* 2014, 6, 11553−11573.

(8) Bordet, A.; Landis, R. F.; Lee, Y.; Tonga, G. Y.; Asensio, J. M.; Li, C.-H.; Fazzini, P.-F.; Soulantica, K.; Rotello, V. M.; Chaudret, B. Water-dispersible and biocompatible iron carbide nanoparticles with high specific absorption rate. *ACS Nano* 2019, 13, 2870−2878.

(9) Hyeon, T. Chemical synthesis of magnetic nanoparticles. *Chem. Commun.* 2003, 927−934.

(10) Hyeon, T.; Lee, S. S.; Park, J.; Chung, Y.; Na, H. B. Synthesis of highly crystalline and monodisperse maghemite nanocrystallites without a size-selection process. *J. Am. Chem. Soc.* 2001, 123, 12798−12801.

(11) Kura, H.; Takahashi, M.; Ogawa, T. Synthesis of monodisperse iron nanoparticles with a high saturation magnetization using an $Fe(CO)_x$-oleylamine reacted precursor. *J. Phys. Chem. C* 2010, 114, 5835−5838.

(12) Zhao, C. X.; He, L.; Qiao, S. Z.; Middelberg, A. P. Nanoparticle synthesis in microreactors. *Chem. Eng. Sci.* 2011, 66, 1463−1479.

(13) Song, Y.; Hormes, J.; Kumar, C. S. S. R. Microfluidic synthesis of nanomaterials. *Small* 2008, 4, 698−711.

(14) Marre, S.; Jensen, K. F. Synthesis of micro and nanostructures in microfluidic systems. *Chem. Soc. Rev.* 2010, 39, 1183−1202.

(15) Luo, G.; Du, L.; Wang, Y.; Lu, Y.; Xu, J. Controllable preparation of particles with microfluidics. *Particuology* 2011, 9, 545−558.

(16) Krishna, K. S.; Li, Y.; Li, S.; Kumar, C. S. S. R. Lab-on-a-chip synthesis of inorganic nanomaterials and quantum dots for biomedical applications. *Adv. Drug Delivery Rev.* 2013, 65, 1470−1495.

(17) Myers, R. M.; Fitzpatrick, D. E.; Turner, R. M.; Ley, S. V. Flow chemistry meets advanced fuctional materials. *Chem. - Eur. J.* 2014, 20, 12348−12366.

(18) Phillips, T. W.; Lignos, I. G.; Maceiczyk, R. M.; deMello, A. J.; deMello, J. C. Nanocrystal synthesis in microfluidic reactors: where next? *Lab Chip* 2014, 14, 3172−3180.

(19) Sebastian, V.; Arruebo, M.; Santamaria, J. Reaction engineering strategies for the production of inorganic nanomaterials. *Small* 2014, 10, 835−853.

(20) Sebastian, V.; Khan, S. A.; Kulkarni, A. Perspective article: flow synthesis of functional materials. *J. Flow Chem.* 2017, 7, 96−105.

(21) Santana, J. S.; Skrabalak, S. E. Continuous flow routes toward designer metal nanocatalysts. *Adv. Energy Mater.* 2020, 10, 1−14.

(22) Roberts, E. J.; Karadaghi, L. R.; Wang, L.; Malmstadt, N.; Brutchey, R. L. Continuous flow methods of fabricating catalytically active metal nanoparticles. *ACS Appl. Mater. Interfaces* 2019, 11, 27479−27502.

(23) Kulkarni, A. A.; Jundale, R. B. Continuous flow synthesis of nanomaterials (Chapter 9 from the book 'Flow chemistry: Integrated

approaches for practical applications'). *RSC Green Chemistry* 2019, 62 (2020), 316−339.

(24) Frenz, L.; El Harrak, A.; Pauly, M.; Bégin-Colin, S.; Griffiths, A. D.; Baret, J. C. Droplet-based microreactors for the synthesis of magnetic iron oxide nanoparticles. *Angew. Chem., Int. Ed.* 2008, 47, 6817−6820.

(25) Larrea, A.; Sebastian, V.; Ibarra, A.; Arruebo, M.; Santamaria, J. Gas slug microfluidics: a unique tool for ultrafast, highly controlled growth of iron oxide nanostructures. *Chem. Mater.* 2015, 27, 4254−4260.

(26) Lee, W. B.; Weng, C. H.; Cheng, F. Y.; Yeh, C. S.; Lei, H. Y.; Lee, G. B. Biomedical microdevices synthesis of iron oxide nanoparticles using a microfluidic system. *Biomed. Microdevices* 2009, 11, 161−171.

(27) Simmons, M.; Wiles, C.; Rocher, V.; Francesconi, M. G.; Watts, P. The preparation of magnetic iron oxide nanoparticles in microreactors. *J. Flow Chem.* 2013, 3, 7−10.

(28) Abou-Hassan, A.; Sandre, O.; Neveu, S.; Cabuil, V. Synthesis of goethite by separation of the nucleation and growth processes of ferrihydrite nanoparticles using microfluidics. *Angew. Chem., Int. Ed.* 2009, 48, 2342−2345.

(29) Lee, S. H. S.; Dawood; Choi, W. K.; Hatton, T. A.; Khan, S. A. Hierarchical materials synthesis at soft all-aqueous interfaces. *Soft Matter* 2012, 8, 3924−3928.

(30) Miyake, T.; Ueda, T.; Ikenaga, N.; Oda, H.; Sano, M. Synthesis of Fe_2O_3 in the capillary-tube reactor. *J. Mater. Sci.* 2005, 40, 5011−5013.

(31) Uson, L.; Arruebo, M.; Sebastian, V.; Santamaria, J. Single phase microreactor for the continuous, high-temperature synthesis of < 4 nm superparamagnetic iron oxide nanoparticles. *Chem. Eng. J.* 2018, 340, 66−72.

(32) Glasgow, W.; Fellows, B.; Qi, T.; Darroudi, T.; Kitchens, C.; Ye, L.; Crawford, T. M.; Mefford, O. T. Continuous synthesis of iron oxide (Fe_3O_4) nanoparticles via thermal decomposition. *Particuology* 2016, 26, 47−53.

(33) Jiao, M.; Zeng, J.; Jing, L.; Liu, C.; Gao, M. Flow synthesis of biocompatible Fe_3O_4 nanoparticles: insight into the effects of residence time, fluid velocity and tube reactor dimension on particle size distribution. *Chem. Mater.* 2015, 27, 1299−1305.

(34) Peng, S.; Wang, C.; Xie, J.; Sun, S. Synthesis and stabilization of monodisperse Fe nanoparticles. *J. Am. Chem. Soc.* 2006, 128, 10676−10677.

(35) Vargeese, A. A. Pressure effects on thermal decomposition reactions: a thermo-kinetic investigation. *RSC Adv.* 2015, 5, 78598−78605.

(36) Carlton, H. E.; Oxley, J. H. Kinetics of the heterogeneous decomposition of iron pentacarbonyl. *AIChE J.* 1965, 11, 79−84.

(37) Wen, J. Z.; Goldsmith, C. F.; Ashcraft, R. W.; Green, W. H. Detailed kinetic modeling of iron nanoparticle synthesis from the decomposition of $Fe(CO)_5$. *J. Phys. Chem. C* 2007, 111, 5677−5688.

(38) Rodriguez-Carvajal, J. Recent Advances in magnetic structure determination by neutron powder diffraction. *Phys. B* 1993, 192, 55−69.

(39) Yao, S.; Yang, C.; Zhao, H.; Li, S.; Lin, L.; Wen, W.; Liu, J.; Hu, G.; Li, W.; Hou, Y.; Ma, D. Reconstruction of the wet chemical synthesis process: the case of Fe_5C_2 nanoparticles. *J. Phys. Chem. C* 2017, 121, 5154−5160.

(40) Yang, Z.; Zhao, T.; Huang, X.; Chu, X.; Tang, T.; Ju, Y.; Wang, Q.; Hou, Y.; Gao, S. Modulating the phases of iron carbide nanoparticles: from a perspective of interfering with the carbon penetration of $Fe@Fe_3O_4$ by selectively adsorbed halide ions. *Chem. Sci.* 2017, 8, 473−481.

(41) Schaefer, Z. L.; Weeber, K. M.; Misra, R.; Schiffer, P.; Schaak, R. E. Bridging hcp-Ni and Ni_3C via a Ni_3C_{1-x} solid solution: tunable composition and magnetism in colloidal nickel carbide nanoparticles. *Chem. Mater.* 2011, 23, 2475−2480.

(42) Yu, J.; Yang, C.; Li, J.; Ding, Y.; Zhang, L.; Yousaf, M. Z.; Lin, J.; Pang, R.; Wei, L.; Xu, L.; Sheng, F.; Li, C.; Li, G.; Zhao, L.; Hou, Y. Multifunctional Fe_5C_2 nanoparticles: a targeted theranostic platform

for magnetic resonance imaging and photoacoustic tomography-guided photothermal therapy. *Adv. Mater.* **2014**, *26*, 4114−4120.

(43) Yin, Y.; Rioux, R. M.; Erdonmez, C. K.; Hughes, S.; Somorjai, G. A.; Alivisatos, P. Formation of hollow nanocrystals through the nanoscale Kirkendall effect. *Science* **2004**, *304*, 711−714.

(44) Park, E.; Zhang, J.; Thomson, S.; Ostrovski, O.; Howe, R. Characterization of phases formed in the iron carbide process by X-ray diffraction, Mössbauer, X-ray photoelectron spectroscopy, and Raman spectroscopy analyses. *Metall. Mater. Trans. B* **2001**, *32*, 839−845.

(45) Raupp, G.; Delgass, W. N. Mössbauer investigation of supported Fe and FeNi catalysts II. Carbides formed Fischer−Tropsch synthesis. *J. Catal.* **1979**, *58*, 348−360.

(46) Amelse, J. A.; Grynkewich, G.; Butt, J. B.; Schwartz, L. H. Mössbauer specroscopic study of passivated small particles of iron and iron carbide. *J. Phys. Chem.* **1981**, *85*, 2484−2488.

(47) Liu, X.-W.; Zhao, S.; Meng, Y.; Peng, Q.; Dearden, A. K.; Huo, C.-F.; Yang, Y.; Li, Y.-W.; Wen, X.-D. Mössbauer spectroscopy of iron carbides: From prediction to experimental confirmation. *Sci. Rep.* **2016**, *6*, 26184.

(48) Mathalone, Z.; Ron, M.; Pipman, J.; Niedzwiedz, S. Mössbauer Characteristics of ε, χ, and θ iron carbides. *J. Appl. Phys.* **1971**, *42*, 687−695.

(49) Le Caër, G.; Dubois, J. M.; Pijolat, M.; Perrichon, V.; Bussiere, P. Characterization by Mössbauer spectroscopy of iron carbides formed by Fischer−Tropsch synthesis. *J. Phys. Chem.* **1982**, *86*, 4799−4808.

(50) Fang, C. M.; van Huis, M. A.; Zandbergen, H. W. Structural, electronic, and magnetic properties of iron carbide Fe_7C_3 phases from first-principles theory. *Phys. Rev. B: Condens. Matter Mater. Phys.* **2009**, *80*, 224108.

(51) Yang, C.; Zhao, H.; Hou, Y.; Ma, D. Fe_5C_2 nanoparticles: a facile bromide-induced synthesis and as an active phase for Fischer−Tropsch synthesis. *J. Am. Chem. Soc.* **2012**, *134*, 15814−15821.

(52) Abel, F. M.; Pourmiri, S.; Basina, G.; Tzitzios, V.; Devlin, E.; Hadjipanayis, G. C. Iron carbide nanoplatelets: colloidal synthesis and characterization. *Nanoscale Adv.* **2019**, *1*, 4476−4480.

(53) Mehta, J. P.; Knappett, B. R.; Divitini, G.; Ringe, E.; Midgley, P. A.; Fairen-Jimenez, D.; Wheatley, A. E. H. Advances in the synthesis and long-term protection of zero-valent iron nanoparticles. *Part. Part. Syst. Charact.* **2018**, *35* (35), 1800120.

(54) Famiani, S.; LaGrow, A. P.; Besenhard, M. O.; Maenosono, S.; Thanh, N. T. K. Synthesis of fine-tuning highly magnetic $Fe@Fe_xO_y$ nanoparticles through continuous injection and a study of magnetic hyperthermia. *Chem. Mater.* **2018**, *30*, 8897−8904.

(55) Meffre, A.; Mehdaoui, B.; Kelsen, V.; Fazzini, P.-F.; Carrey, J.; Lachaize, S.; Respaud, M.; Chaudret, B. A simple chemical route toward monodisperse iron carbide nanoparticles displaying tunable magnetic and unprecedented hyperthermia properties. *Nano Lett.* **2012**, *12*, 4722−4728.

(56) Bordet, A.; Lacroix, L.-M.; Fazzini, P.-F.; Carrey, J.; Soulantica, K.; Chaudret, B. Magnetically induced continuous CO_2 hydrogenation using composite iron carbide nanoparticles of exceptionally high heating power. *Angew. Chem., Int. Ed.* **2016**, *55*, 15894−15898.

(57) Gao, J.; Wang, X.; Pan, X.; Ren, X.; Han, Y.; Yang, X.; Yang, Y. Facile synthesis of nanocrystalline Fe/Fe_3C induced by bromide. *J. Mater. Sci.: Mater. Electron.* **2016**, *27*, 64−69.

(58) Yu, J.; Chen, F.; Gao, W.; Ju, Y.; Chu, X.; Che, S.; Sheng, F.; Hou, Y. Iron carbide nanoparticles: an innovative nanoplatform for biomedical applications. *Nanoscale Horiz.* **2017**, *2*, 81−88.

(59) Ye, Z.; Zhang, P.; Lei, X.; Wang, X.; Zhao, N.; Yang, H. Iron Carbides and Nitrides: Ancient Materials with Novel Prospects. *Chem. - Eur. J.* **2018**, *24*, 8922−8940.

(60) Ye, Z.; Qie, Y.; Fan, Z.; Liu, X.; Shi, Z.; Yang, H. Soft magnetic Fe_5C_2-$Fe_3C@C$ as an electrocatalyst for the hydrogen evolution reaction. *Dalton Trans.* **2019**, *48*, 4636−4642.

(61) Asensio, J. M.; Marbaix, J.; Mille, N.; Lacroix, L.-M.; Soulantica, K.; Fazzini, P.-F.; Carrey, J.; Chaudret, B. To Heat or not to Heat: a Study of the Performances of Iron Carbide Nanoparticles in Magnetic Heating. *Nanoscale* **2019**, *11*, 5402−5411.

(62) Gazeau, F.; Lévy, M.; Wilhelm, C. Optimizing magnetic nanoparticle design for nanothermotherapy. *Nanomedicine* **2008**, *3*, 831−844.

(63) Blanco-Andujar, C.; Walter, A.; Cotin, G.; Bordeianu, C.; Mertz, D.; Felder-Flesch, D.; Begin-Colin, S. Design of iron oxide-based nanoparticles for MRI and magnetic hyperthermia. *Nanomedicine* **2016**, *11*, 1889−1910.